Near-infrared absorbing 2D/3D ZnIn$_2$S$_4$/N-doped graphene photocatalyst for highly efficient CO$_2$ capture and photocatalytic reduction

Yang Xia[1], Bei Cheng[1], Jiajie Fan[2], Jiaguo Yu[1,2*] and Gang Liu[3*]

ABSTRACT Hierarchical heterostructure photocatalysts with broad spectrum solar light utilization, particularly in the near-infrared (NIR) region, are emerging classes of advanced photocatalytic materials for solar-driven CO$_2$ conversion into value-added chemical feedstocks. Herein, a novel two-demensional/three-demensional (2D/3D) hierarchical composite is hydrothermally synthesized by assembling vertically-aligned ZnIn$_2$S$_4$ (ZIS) nanowall arrays on nitrogen-doped graphene foams (NGF). The prepared ZIS/NGF composite shows enhancement in photothermal conversion ability and selective CO$_2$ capture as well as solar-driven CO$_2$ photoreduction. At 273 K and 1 atm, the ZIS/NGF composite with 1.0 wt% NGF achieves a comparably high CO$_2$-to-N$_2$ selectivity of 30.1, with an isosteric heat of CO$_2$ adsorption of 48.2 kJ mol^{-1}. And in the absence of cocatalysts and sacrificial agents, the ZIS/NGF composite with cyclability converts CO$_2$ into CH$_4$, CO and CH$_3$OH under simulated solar light illumination, with the respective evolution rates about 9.1, 3.5, and 5.9 times higher than that of the pristine ZIS. In-depth analysis using *in-situ* irradiated X-ray photoelectron spectroscopy (ISI-XPS) in conjunction with Kelvin probe measurements reveals the underlying charge transfer pathway and process from ZIS to NGF.

Keywords: near-infrared light, nitrogen-doped graphene foams, ZnIn$_2$S$_4$ nanowalls, selective CO$_2$ capture, CO$_2$ photocatalytic reduction

INTRODUCTION

The growing energy demand by mankind largely relies on fossil fuel combustion that has been producing huge amounts of carbon dioxide (CO$_2$), a so-called anthro- pogenic greenhouse gas. Reducing CO$_2$ levels in the atmosphere and combating global warming and its associated climate change is one of the crucial challenges in the 21st century. To this end, sunlight-driven CO$_2$ conversion into value-added chemicals and/or fuels has shown great potential to solve the ongoing serious environmental issue [1–9]. Since the pioneer research by Halmann in 1978, diverse semiconductor-based photocatalysts have been developed for CO$_2$ reduction with water [10–16]. To date, the efficiencies of CO$_2$ conversion are well below the expected levels for practical applications, due to the fast recombination of the photogenerated charge carriers, the limited light absorption ability of the photocatalysts as well as the sluggish CO$_2$ adsorption and diffusion [17–22]. This clearly exemplifies the urgent need for the development of advanced photocatalytic materials for achieving high performance in CO$_2$ photoreduction.

Among newly emerged semiconducting photocatalysts, metal sulfides and their associated composites have been examined for CO$_2$ conversion due to their distinct electronic and optical characteristics, strong light harvesting ability as well as excellent recyclability [23–26]. Especially, the modification of metal sulfides with carbon-base materials, including graphene [27,28], carbon nanotube [29,30], and carbon quantum dots [31,32], is considered to be one of the most efficient approaches to achieve efficient photocatalytic CO$_2$ conversion. Nevertheless, the vast majority of carbon-based materials suffer from aggregation due to the inherent van der Waals interactions. On the other hand, three-dimensional (3D) graphene nanostructures composed of 2D graphene sheets have

[1] State Key Laboratory of Advanced Technology for Materials Synthesis and Processing, Wuhan University of Technology, Wuhan 430070, China
[2] School of Materials Science and Engineering, Zhengzhou University, Zhengzhou 450001, China
[3] CAS Key Laboratory of Standardization and Measurement for Nanotechnology, CAS Center for Excellence in Nanoscience, National Center for Nanoscience and Technology, Beijing 100190, China
* Corresponding authors (emails: yujiaguo93@whut.edu.cn (Yu J); liug@nanoctr.cn (Liu G))

been intensively studied in energy storage [33–35], environmental remediation [36–38], and gas sensing [39–41]. Compared with 2D graphene counterparts, 3D graphene nanostructures can hold interconnected networks with more surface areas and active sites in addition to hierarchical frameworks, which make them an ideal scaffold to inhibit the aggregation or stacking of subunits [42–46]. Further, doping heteroatoms like N into 3D graphene may significantly modify the electronic structure as well as benefit the intimate contact between graphene with dissimilar materials [47–50]. In this regard, combining 3D nitrogen-doped graphene with metal sulfides for efficient CO_2 conversion is appealing.

Herein, for the first time, we hydrothermally synthesized a novel 2D/3D hierarchical composite by assembling vertically-aligned $ZnIn_2S_4$ (ZIS) nanowall arrays on nitrogen-doped graphene foams (NGF). The as-synthesized ZIS/NGF mixed-dimensional composites were shown to boost light absorption from UV to near-infrared (NIR) region, charge carrier separation, and selective CO_2-to-N_2 uptake. Under simulated solar light illumination, the ZIS/NGF composites converted CO_2 into CH_4, CO and CH_3OH more efficiently in comparison with the pristine ZIS. On the basis of systematic characterization including *in-situ* irradiated X-ray photoelectron spectroscopy (ISI-XPS), the synergistic effects towards CO_2 conversion between ZIS and NGF were uncovered.

EXPERIMENTAL SECTION

Synthesis of NGF
Graphene oxide (GO) was prepared from natural graphite powder by a modified Hummers method [51]. 3D NGF was synthesized through a facile method as following. Typically, 100 mg GO was dispersed in 50 mL solution composed of ethanol and deionized water in a 1:1 volume ratio to obtain a homogeneous suspension. A precleaned commercial polyurethane (PU) sponge was immersed into the GO suspension and pressed for several times to enhance the diffusion of GO sheets into the sponge. The PU sponge loaded with GO was dried at 80°C and then annealed in a furnace at 350°C for 10 min.

Synthesis of ZIS/NGF heterojunction
The ZIS/NGF composites were hydrothermally prepared by coupling $ZnIn_2S_4$ nanowalls with 3D NGF. Typically, 0.25 mmol of $Zn(CH_3COO)_2·2H_2O$, 0.50 mmol of $In(NO_3)_3·6H_2O$ were added into a solvent containing 20 mL water and 10 mL ethanol. Then a certain amount of 3D NGF was immersed in the above solution under

slow magnetic stirring for 30 min. Next, 4.0 mmol of *L*-cysteine was dispersed into the mixture. The mixed solution was transferred into a 50-mL Teflon-lined autoclave and maintained at 160°C for 12 h. After cooling down to room temperature, the obtained blackish green suspension was repeatedly washed by water and ethanol for several times, and then dried in vacuum oven at 60°C for 12 h to obtain the ZIS/NGF composites. Herein, the nominal weight percentage of NGF is 0.5, 1.0, 3.0 and 5.0 wt%, which is denoted as ZIS/NGF0.5, ZIS/NGF1, ZIS/NGF3 and ZIS/NGF5, respectively. Moreover, pristine ZIS was prepared under the same conditions except in the absence of the nitrogen-doped graphene foams. For comparison, we also prepared a ZIS/GO1 composite with the GO weight percentage of 1.0 wt%.

Material characterizations
The crystalline structures of the samples were probed by an X-ray diffractometer with Cu Kα radiation (Rigaku, Japan). The morphology and energy dispersive X-ray spectroscopy (EDX) elemental mapping were examined by field emission scanning electron microscopy (FESEM, JSM-7500, JEOL) and transmission electron microscopy (TEM, G2 60-300, Titan). Nitrogen adsorption-desorption isotherms were obtained by Micromeritics ASAP 2020 at 77 K. Prior to the measurements, the samples were degassed at 150°C for 12 h under vacuum and nitrogen atmosphere. Both Brunauer-Emmett-Teller (BET) surface area (S_{BET}) and pore sizes were calculated from the desorption branch of isotherms according to the BJH method. UV−vis−NIR diffuse reflectance spectra (DRS) were recorded on a Shimadzu UV-2600 UV–vis spectrophotometer (Japan) using $BaSO_4$ as a reference. XPS measurements were conducted on a VG EXCALAB 210 instrument with Al Kα X-ray radiation. ISI-XPS measurements were carried out on a VG EXCALAB 210 instrument with Al Kα X-ray radiation under a 3 W UV-LED (light-emitting diode) (365 nm) light irradiation. The Fourier transform infrared (FTIR) spectra of the samples were recorded by an IR Affnity-1 FTIR spectrometer. Raman spectra were measured at room temperature by using a micro-Raman spectrometer (Renishaw InVia) in the backscattering geometry with a 514.5-nm Ar^+ laser as an excitation source. Photoluminescence (PL) spectra were recorded at room temperature using a fluorescence spectrophotometer (F-7000, Hitachi, Japan) with a 380 nm excitation wavelength. Time-resolved photoluminescence (TRPL) decay curves were measured using an FLS1000 fluorescence lifetime spectrophotometer (Edinburgh Instruments, UK) under

375 nm light excitation. The photoelectrochemical measurements were carried out on a CHI660C electrochemical analyzer in 0.5 mol L^{-1} Na$_2$SO$_4$ solution with a homemade three-electrode quartz cell, using a Pt wire and Ag/AgCl electrode serving as the counter electrode and reference electrode, respectively. The catalyst was coated onto a fluorine-doped tin oxide (FTO) glass, which was used as the working electrode. The electrochemical impedance spectra (EIS) and photoresponse–time curves were recorded at open circuit potential. The irradiation source was a 3 W UV-LED (365 nm). A Kelvin probe apparatus (Instytut Fotonowy, Poland) with a sensitivity of 1 mV was employed to detect contact potential differences (CPDs) using a gold mesh Kelvin probe (3 mm diameter, Instytut Fotonowy, Poland) as the reference. The surface work function was monitored using an LED lamp as a light source in conjunction with a monochromator. The CPD signal was monitored as a function of illumination time.

CO$_2$ and N$_2$ adsorption measurements
CO$_2$ adsorption measurements were carried out up to 1 bar at 273 K (ice-water bath) and 298 K (room temperature) on a Quantachrome Quadrasorb SI apparatus. Prior to adsorption, the samples were degassed at 150°C under vacuum for 12 h. The same test procedure was adapted for the N$_2$ adsorption measurements at 273 K.

The selectivity (S_{IAST}) for a binary gas mixture containing CO$_2$ and N$_2$ was calculated based on the Ideal Adsorption Solution Theory (IAST) and is defined as following:

$$S_{IAST} = \frac{q_{CO_2}/q_{N_2}}{P_{CO_2}/P_{N_2}}, \tag{1}$$

where q_{CO_2} and q_{N_2} are the respective molar loading (mmol g^{-1}) of CO$_2$ and N$_2$; P_{CO_2} and P_{N_2} are the partial pressure of CO$_2$ and N$_2$, respectively.

Photocatalytic CO$_2$ reduction
All of the samples were degassed at 150°C for 6 h prior to the measurements. Specifically, a 200-mL customized glass flask with two-neck was used as reactor. 0.1 g of the degassed sample was added to the reactor, dispersed in 10 mL deionized water by ultrasonication, and then dried at 80°C to form a smooth and thin film on the bottom of the reactor. 0.084 g of NaHCO$_3$ was added to the neck of reactor, and N$_2$ was blown through the reactor to ensure anaerobic conditions before light irradiation. H$_2$SO$_4$ aqueous solution (0.3 mL, 2.0 mol L^{-1}) was syringed into the reaction system to produce CO$_2$ and H$_2$O sources. A

300 W Xe lamp was employed as the light source. After the reactor system was irradiated for 1 h, the resulting products were detected by a gas chromatography (GC-2014C, Shimadzu, JAPAN). To investigate the stability of the sample ZIS/NGF1 on CO$_2$ conversion, the sample was collected after each photocatalytic reduction reaction for 3 h and recycled for 3 runs with the same procedure.

A ^{13}CO$_2$ isotope tracer experiment was performed to determine the origin of the photocatalytic CO$_2$ reduction products over the prepared samples. In detail, ^{12}C and ^{13}C isotope labeled NaHCO$_3$ and H$_2$SO$_4$ aqueous solution was used to generate the ^{12}CO$_2$ and ^{13}CO$_2$. After the photocatalytic reaction for 1 h, 500 mL of mixed gas was injected into a gas chromatography-mass spectrometer (GC-MS) (6980N network GC system–5975 inert mass selective detector, Agilent Technologies, USA) to analyze the products.

The intermediate products generated during the photocatalytic CO$_2$ reduction over the ZIS/NGF composite were probed *via in situ* diffuse reflectance infrared Fourier transform spectroscopy (DRIFTS). Firstly, the obtained sample was degassed at 150°C for 12 h. Then, the pretreated sample was placed at the bottom of the DRIFTS sealed chamber. Subsequently, a mixed gas of CO$_2$ and H$_2$O vapor was introduced into the chamber. The DRIFTS spectra were obtained either in dark or under 3 W UV–LED light (365 nm) irradiation.

RESULTS AND DISCUSSION
The NGF was synthesized using a template-assisted strategy by burning GO-adsorbed polyurethane sponge (PU). Upon adding Zn(CH$_3$COO)$_2$ and In(NO$_3$)$_3$ solution, both Zn^{2+} and In^{3+} ions were adsorbed on the surface of NGF *via* static electric interaction. Subsequently, L-cysteine releases S^{2-} ions into the solution to react with the Zn^{2+} and In^{3+} to form ZnIn$_2$S$_4$ crystallites, which continue to nucleate and grow into the ZnIn$_2$S$_4$/NGF composite as shown in Scheme 1. The morphologies and microstructures of the prepared samples were characterized by FESEM. As presented in Fig. 1a, the NGF shows a 3D network structure with abundant micrometer-sized pores. A close look into the 3D network by the inset of Fig. 1a reveals graphene scaffolds with curly sheets. Upon hydrothermal treatment, ZIS nanowalls are anchored on the surface of 3D NGF and the 3D network structure of NGF is well intact (Fig. 1b). Indeed, the lamellar ZIS nanowalls are vertically aligned on the surface of NGF to form a 2D/3D mixed-dimensional architecture (inset of Fig. 1b). In contrast, the pristine ZIS nanowalls present homogeneously distributed flower-like microspheres with
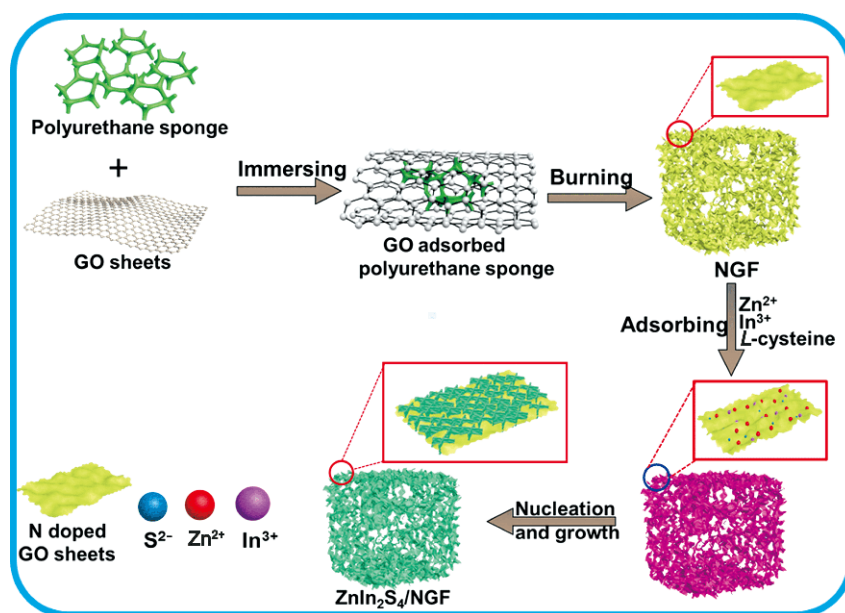
Scheme 1 Schematic illustration for the formation process of hierarchical 2D/3D ZnIn₂S₄/NGF composite.
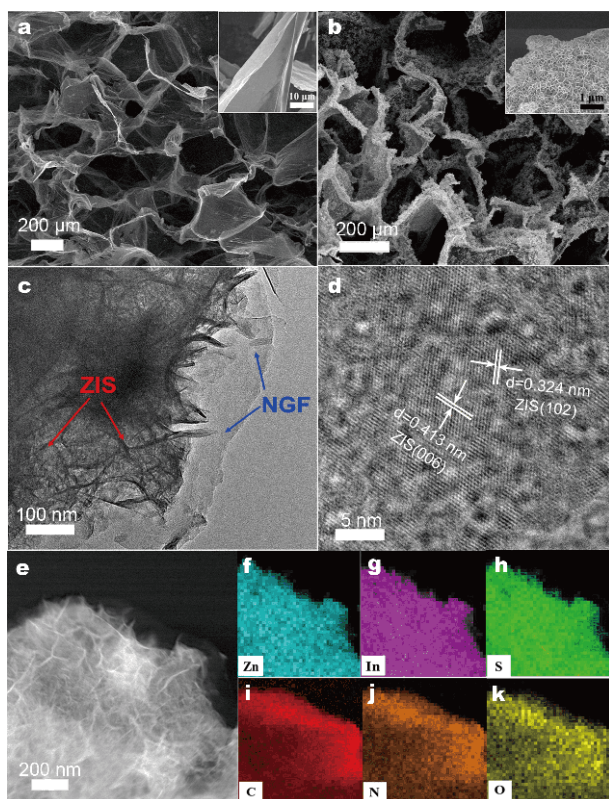

Figure 1 Typical FESEM images of (a) NGF and (b) ZIS/NGF. Insets: the high-magnification FESEM images. (c) TEM and (d) HRTEM images of ZIS/NGF. (e) STEM image of ZIS/NGF and (f–k) the corresponding elemental mapping images of Zn, In, S, C, N, and O.

a diameter of 2–3 μm that are composed of numerous petals (Fig. S1). Therefore, the above results illustrate that the NGF plays a key role on the morphology of ZIS in the formation process of ZIS/NGF composites that are expected to facilitate the transfer of charge carriers between the ZIS nanowalls and NGF. Fig. 1c displays a typical low-magnification TEM image of the ultrathin ZIS nanowalls supported on the surface of NGF.

The corresponding *d*-spacings of the lattice fringes characterized by high-resolution TEM (HRTEM) are measured to be 0.324 and 0.413 nm, in accordance with the (102) and (006) crystal plane of hexagonal ZIS (Fig. 1d), respectively. Additionally, a representative high-angle annular dark-field scanning transmission electron microscopy (HAADF-STEM) image (Fig. 1e) and the corresponding EDX elemental mappings (Fig. 1f–k) of ZIS/NGF reveal the homogeneous distribution of Zn, In, S, C, N and O elements. Such results prove the formation of hierarchical 2D/3D composites between ZIS nanowalls and NGF network.

The identification of ZIS, NGF and ZIS/NGF structures was conducted using X-ray diffraction (XRD) patterns as shown in Fig. 2a. The diffraction peaks of pristine ZIS at 22.1°, 27.7°, 47.3°, 52.4° and 55.8° can be indexed to (006), (102), (110), (116) and (022) planes of hexagonal phase (JCPDS 72-0773), respectively [52–54]. The NGF gives one broad diffraction peak at 21.5° that can be ascribed to the diffraction characteristic of graphite [55]. Typical
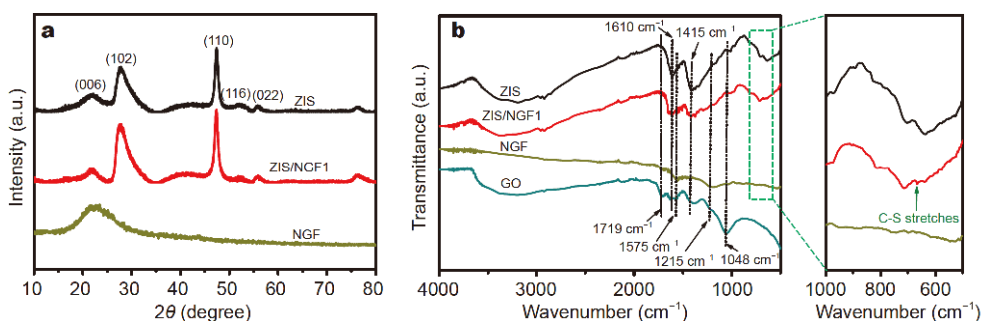
Figure 2 (a) XRD patterns of ZIS, NGF and ZIS/NGF samples. (b) FT-IR spectra of ZIS, GO, NGF and ZIS/NGF1 samples.

ZIS/NGF composites like ZIS/1.0 wt% NGF (denoted as ZIS/NGF1) exhibit comparable XRD patterns with ZIS, which is mainly due to the relatively low content of NGF. Apparently, the peak intensities of ZIS/NGF1 increase in comparison with those of pristine ZIS, implying that the combination of NGF with ZIS facilitates the nucleation and crystallization of ZIS. The chemical structure of the as-prepared specimens was investigated by FTIR and Raman measurement. Fig. 2b displays the FTIR spectra of graphene oxide (GO), ZIS, NGF, and ZIS/NGF samples. The characteristic peaks of GO at 1719, 1575, 1215 and 1048 cm^{-1} are assigned to the C=O stretching vibration mode of carboxyl, C=C stretching, O–H bending and phenolic C–OH stretching vibration modes, respectively [56,57]. The peaks of ZIS and GO at 1610 and 1415 cm^{-1} are ascribed to water molecules and hydroxyl groups, respectively.

When constructing NGF *via* calcination, the peaks related to those water molecules and hydroxyl groups are absent. On the other hand, the ZIS/NGF1 composite presents characteristic peaks at 1575, 1215 and 1048 cm^{-1} corresponding to the C=C stretching, O–H bending and phenolic C–OH stretching vibration modes, respectively [58,59]. Furthermore, compared with GO and NGF, no apparent peak related to the C=O vibration mode at 1719 cm^{-1} appears in the ZIS/NGF1 composite with the relatively low content of NGF. Instead, a new peak appears at 665 cm^{-1} for the ZIS/NGF1 composite, which is umbiguously assigned to the C−S stretching mode [60,61]. The Raman spectra of GO, NGF, ZIS and ZIS/NGF samples are displayed in Fig. S2. It is clear that GO, NGF and ZIS/NGF display D band (1359 cm^{-1}) and G band (1588 cm^{-1}), which is attributed to the defects and the disordered C atoms and the E_{2g} vibrational mode of the in-plane C–C sp^2 bond structure, respectively. Compared with the GO, the D and G bands of bare NGF show blue-shifts due to N doping. On the other hand, the D and G bands of ZIS/NGF are shifted to higher wave-

numbers as compared with bare NGF, suggesting the chemical interactions between ZIS and NGF. The intensity ratio (I_D/I_G) between the D and G bands often represents the disorder degree of carbon-based materials [62]. It is notable that the I_D/I_G value of ZIS/NGF is 1.12 that is greater than that of NGF (1.04) and GO (0.86), indicating that the oxygen-containing functional groups in the NGF have been removed, and defects have been introduced into the ZIS/NGF during the process of calcination and hydrothermal treatment.

To further probe the chemical interactions between ZIS and NGF, XPS analyses were performed and the results are shown in Fig. 3. The XPS survey spectra (Fig. 3a) show that the typical NGF sample contains C, N and O species, whereas both ZIS and ZIS/NGF1 samples present Zn, In, S, C and O elements. The C and O elements in ZIS probably result from the adsorbed H_2O and CO_2. No N species in the ZIS/NGF1 sample was detected due to the relatively low N content. As for the C 1s core-levels of NGF, high-resolution XPS spectrum (Fig. 3b) exhibits three peaks at 284.8 (surface adventitious carbon), 285.9 (epoxy/hydroxyl), and 287.4 eV (carbonyl), respectively. The corresponding N 1s spectra of NGF as shown in Fig. 3c demonstrate multiple N species like N (398.6 eV), pyrrolic N (399.7 eV), graphitic N (400.5 eV), and N oxide (401.8 eV). Fig. 3d–f display the characteristic doublets located at 1021.8 and 1044.9 eV (Zn 2p), 444.7 and 452.3 eV (In 3d), 161.4 and 162.6 eV (S 2p) for ZIS. Upon coupling NGF and ZIS to form the composite, the Zn 2p, In 3d, and S 2p core-levels are positively shifted by ~ 0.20 eV, while the C 1s core-levels are negatively shifted by ~ 0.25 eV, indicating chemical interactions between ZIS and NGF and associated electron transfer from ZIS to NGF [63]. The *in-situ* irradiated XPS spectra in Fig. 3b–f will be analyzed in conjunction with Kelvin probe measurements to reveal the underlying interfacial charge transfer pathway and process in the following section.

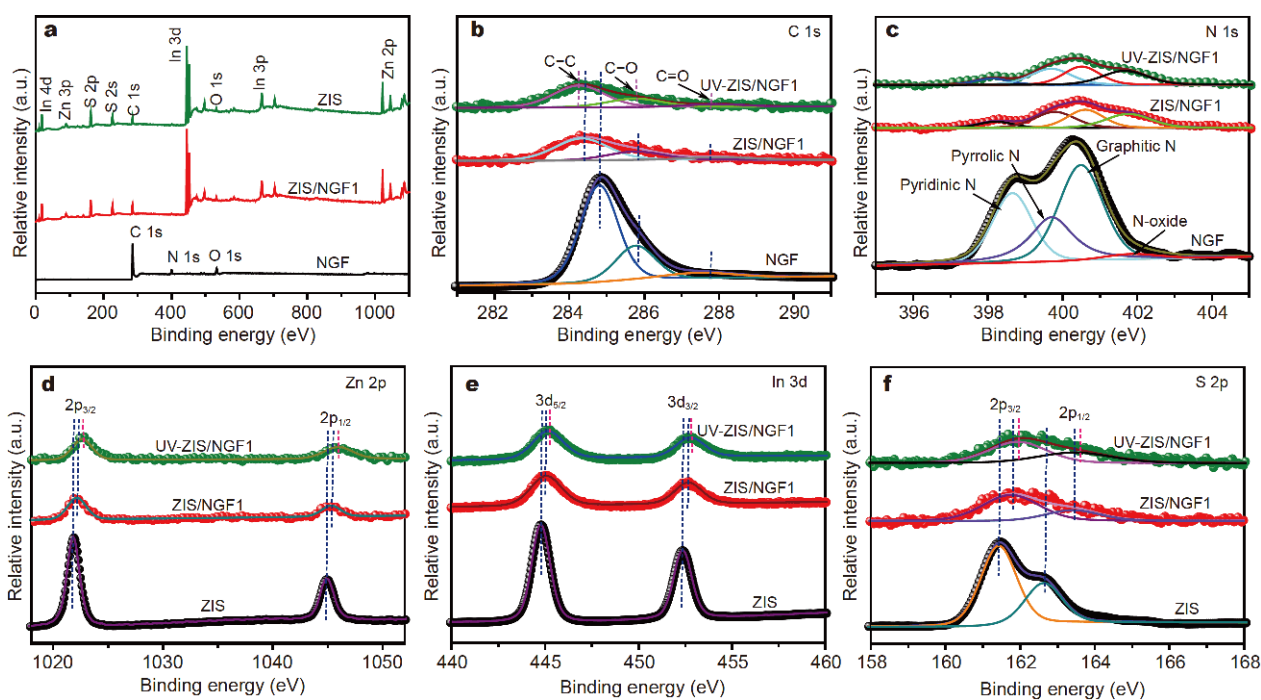In general, photocatalytic materials with large specific

Figure 3 (a) XPS survey spectra of ZIS, NGF, and ZIS/NGF1. High-resolution XPS spectra for (b) C 1s and (c) N 1s of NGF and ZIS/NGF1 either in dark or under 365 nm LED irradiation (denoted UV-ZIS/NGF1). High-resolution XPS spectra of (d) Zn 2p, (e) In 3d, and (f) S 2p core-levels of ZIS and ZIS/NGF1 either in dark or under 365 nm LED irradiation (denoted as UV-ZIS/NGF1).

surface areas may benefit the molecular adsorption and offer abundant active sites for specific photocatalytic reactions. For comparison, we also prepared a ZIS/GO composite in which the weight percentage of GO was 1.0 wt% (denoted as ZIS/GO1). The S_{BET} was determined by N_2 adsorption-desorption isotherm. Fig. 4a displays the specific surface areas and pore size distribution of ZIS, ZIS/GO1 and ZIS/NGF1. All the samples present a type IV isotherm with H3 type hysteresis loops in a relative pressure ranging from 0.45 to 1.0 according to the Brunauer-Deming-Deming-Teller (BDDT) classification [64], indicating the presence of slit-like pores caused by nanowall aggregation. Additionally, enhanced adsorption in the range up to 1.0 is ascribed to large mesopores and macropores. The corresponding pore size distribution curves are shown in the inset of Fig. 4a. All samples exhibit wide pore size distribution from 2 to >100 nm, suggesting the co-existence of both mesopores and macropores. Remarkably, upon coupling NGF with ZIS, the pore size of mesopores becomes larger, which is attributed to the stacking of ZIS nanowalls on the surface of the NGF [56]. Table S1 lists the specific surface area, pore volume and pore size of the samples. Apparently, both specific surface area and pore volume gradually increase with the increasing NGF content, in accordance with the

uniform growth of ultrathin $ZnIn_2S_4$ nanowalls onto NGF with relatively high surface area. However, the specific surface area and the size of mesopores for ZIS/NGF1 are larger than those of ZIS/GO1 due to the uncovered surface inside the graphene foams. The optical absorption properties of the samples were evaluated by UV−vis−NIR DRS. As displayed in Fig. 4b, the ZIS and NGF exhibit a very broad absorption from UV to NIR region. With increasing NGF content, the UV/vis/NIR harvesting capability of ZIS/NGF composites was greatly improved as compared with ZIS. Nevertheless, all samples exhibit absorption edges comparable to that of ZIS. Based on the transformed Kubelka-Munk function [65], the band gap for pure ZIS and ZIS/NGF1 was measured to be ~ 2.58 eV (inset of Fig. 4b). It is reasonable to hypothesize that NGF is not incorporated into the lattice of ZIS which only provides a template to immobilize ZIS. Although a very broad and forceful range of light absorption from 480 to 1400 nm is not able to excite the charge carriers in ZIS, it may still promote the surface catalytic reaction by converting light to heat to activate the catalyst due to the photothermal conversion characteristics of NGF [66]. To authenticate this conjecture, the temperature distribution of the samples was measured by a thermos-image. From Fig. S3, it can be found that the average temperature of
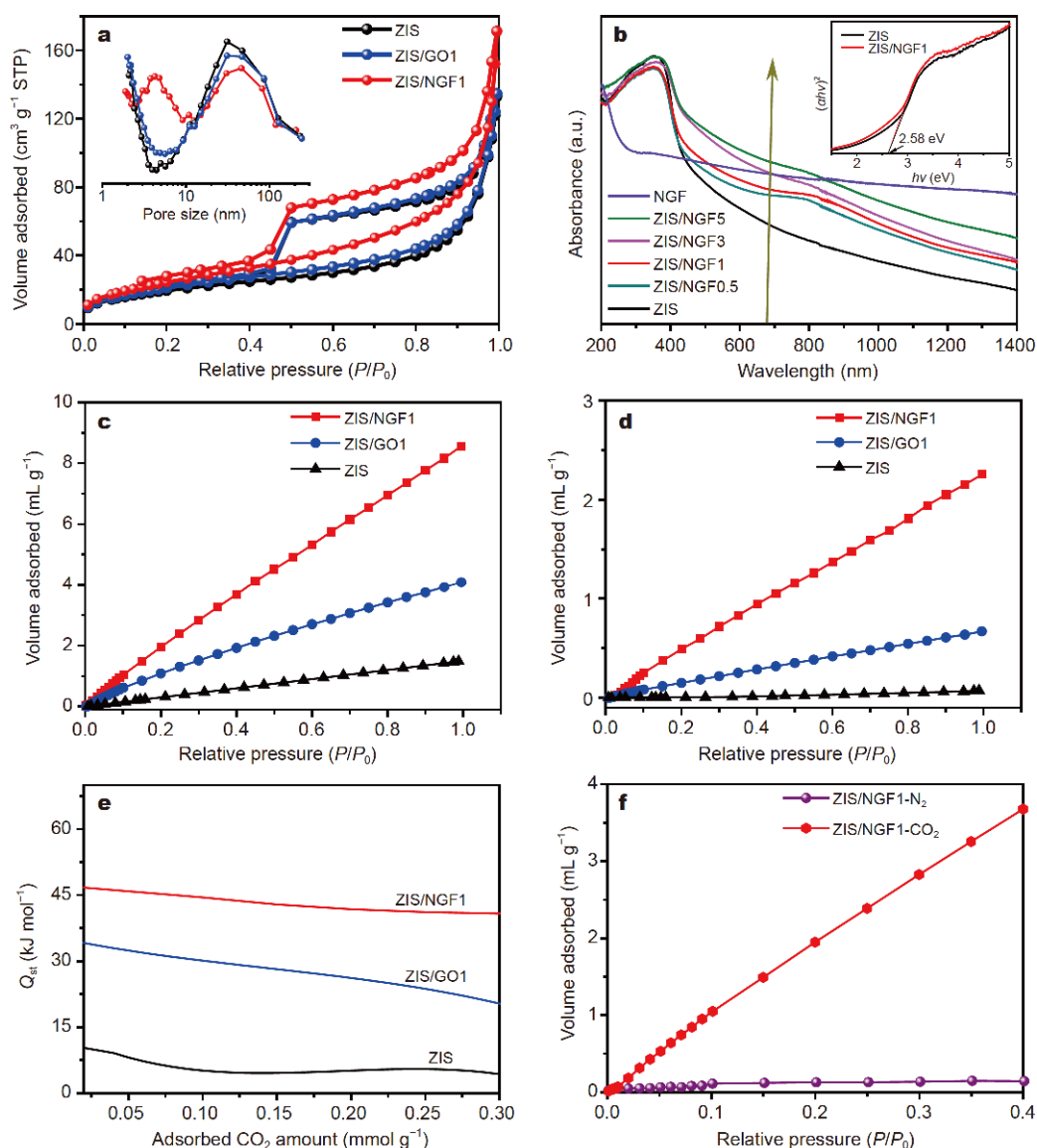
Figure 4 (a) N_2 adsorption-desorption isotherms and pore-size distributions (inset) of ZIS, ZIS/GO1, and ZIS/NGF1. (b) UV-vis-NIR diffusive reflectance spectra of the as-prepared photocatalysts and the corresponding plots (inset) of transformed Kubelka-Munk function *vs.* photon energy of ZIS and ZIS/NGF1. CO_2 adsorption isotherms for ZIS, ZIS/GO1 and ZIS/NGF1 at (c) 273 K and (d) 298 K. (e) The corresponding isosteric heats of CO_2 adsorption on ZIS, ZIS/GO1 and ZIS/NGF1 calculated from the adsorption isotherms at 273 and 298 K. (f) Adsorption isotherms of CO_2 and N_2 on CNNA/rGO at 273 K and 1 atm.

ZIS increases slightly (only 0.2°C) after illuminated by a 760 nm LED light source (3 W), while the average temperature of ZIS/NGF and NGF surfaces increases by 1.0 and 1.2°C after 10 s illumination, respectively. Therefore, this distinction suggests the occurrence of NIR light-induced photothermal conversion effect on the surface of ZIS/NGF.

The CO_2 capture of the as-prepared samples was carried out to evaluate their potential for CO_2 conversion. Fig. 4c, d show the CO_2 adsorption isotherms for ZIS,

ZIS/GO1 and ZIS/NGF1 at 273 and 298 K, respectively. The ZIS/NGF1 composite exhibits higher CO_2 adsorption capacity than ZIS and ZIS/GO1. Remarkably, ZIS/NGF1 shows a much greater temperature dependence of CO_2 adsorption capacity than ZIS/GO1 and ZIS. The above results prove that the larger specific surface area and pores are beneficial to CO_2 uptake [19]. To quantify CO_2 adsorption, the isosteric heat (Q_{st}) at both 273 and 298 K was calculated on the basis of the Clausius-Clapeyron equation [67,68]. As shown in Fig. 4e, the Q_{st} value in the

initial adsorption stage for ZIS/NGF1 is up to 48.2 kJ mol^{-1} that is higher than those of ZIS/GO1 (35.6 kJ mol^{-1}) and ZIS (11.8 kJ mol^{-1}), indicating a much stronger CO_2 chemisorption on ZIS/NGF1 than ZIS/GO1 and ZIS. Accordingly, doping N species into the carbon skeleton of graphene can significantly alter the electronic distribution of the carbon surface, which in turn increases the surface polarity of the carbon materials, thereby leading to much stronger adsorption between CO_2 molecules and ZIS/NGF1 [69,70]. In general, the selective uptake of CO_2 over other gases is highly desirable in practical applications, such as large-scale CO_2 capture from flue gas. Herein, we examined the CO_2-to-N_2 selectivity on ZIS/NGF1. As shown in Fig. 4f, the CO_2 uptake increases sharply as the pressure increases, while the N_2 adsorption capacity only slightly increases in the same pressure range. The selectivity of CO_2 over N_2 gas (i.e., the ratio of the initial slopes of CO_2 and N_2 adsorption isotherms) based on the ideal adsorption solution theory, is calculated to be 30.1 for ZIS/NGF1 that is even comparable to those values of porous polymer network-based [71] and MOF-based materials [67]. Again, the aforementioned results exemplify the strong interactions between CO_2 and polar sites associated with nitrogen-containing groups [71,72]. In other words, the ZIS/NGF composite with large specific surface area and polar sites facilitates CO_2 adsorption, a key step in the surface catalytic reaction kinetics. In particular, the intimate contact between a specific photocatalyst and water molecules may promote CO_2 reduction in that water acts as a proton source and electron donor. Herein, contact angle measurements were conducted and the results in Fig. S4 show that ZIS/NGF1 displays a contact angle of 38° that is smaller than those of ZIS/GO1 (54°) and ZIS (61°), illustrating that doping nitrogen promotes the surface hydrophilicity of GO and hence promote efficient internal electron migration to participate in the CO_2 reduction reactions.

In the absence of any sacrificial agent, the photocatalytic performances of all as-prepared samples were evaluated towards photocatalytic CO_2 reduction in anaerobic environment under simulated sunlight irradiation. The controlled experiments were firstly performed and no hydrocarbons could be detected without photocatalyst, CO_2 and light irradiation, respectively. Fig. 5a and Table S2 show the rates of the major products (CO, CH_4 and CH_3OH) over various samples. ZIS is relatively inactive to the CO_2 reduction, with the respective CH_4, CO and CH_3OH rate of 0.11, 0.70 and 0.23 μmol g^{-1} h^{-1}. As for the ZIS/NGF composite, the

respective rate of CH_4, CO and CH_3OH is first significantly increased and then decreased as a function of NGF amount. ZIS/NFG1 displays the maximum CH_4, CO and CH_3OH rate of 1.01, 2.45 and 1.37 μmol g^{-1} h^{-1}, which is 9.1, 3.5 and 5.9 times as high as that of ZIS, respectively. The photocatalytic performance of ZIS/NFG1 is comparable to other graphene-based photocatalysts reported in the literature (Table S3) for CO_2 photoreduction. For comparison, CO_2 reduction over ZIS/GO1 was also examined under the identical experimental conditions. The respective rate of CH_4, CO and CH_3OH is only 0.40, 1.21 and 0.86 μmol g^{-1} h^{-1}. In addition, both O_2 and H_2 species were also detected on ZIS/NFG1 (Fig. S5 and Table S2). In this system, the production of O_2 from water oxidation is the sole reaction to consume the photogenerated holes, CO_2 is reduced by accepting H^+ and e$^-$ to generate CH_4, CO and CH_3OH. We calculated that the detected yield of O_2 was 7.11 μmol g^{-1} h^{-1} from CO_2 photoreduction over ZIS/NGF1, which is higher than that of the stoichiometric yield (5.62 μmol g^{-1} h^{-1}). This deviation is reasonable within experimental errors and might be related to the undetectable species beyond the GC limitation. However, the rate of H_2 is much lower than the conversion of CO_2, which indicates that the high selective CO_2 capture is in favour of CO_2 photoreduction in this sacrificial agent-free system. In order to verify the origins of the products, the isotope tracer experiment was performed through photocatalytic reduction of either ^{12}C- or ^{13}C-labeled CO_2 under the identical reaction conditions. Fig. 5b, c and Fig. S6a show that the respective charge-mass ratio of 16 (m/z=16), 28 (m/z=28) and 32 (m/z=32) is ascribed to $^{12}CH_4$, ^{12}CO and $^{12}CH_3OH$ derived from $^{12}CO_2$, while the respective charge-mass ratio of 17 (m/z=17), 29 (m/z=29) and 33 (m/z=33) is attributed to $^{13}CH_4$, ^{13}CO and $^{13}CH_3$ OH from $^{13}CO_2$. The above results demonstrate that the carbon source of CH_4, CO and CH_3OH indeed originates from the target CO_2. Furthermore, the photostability was investigated by operating the photocatalytic CO_2 reduction over ZIS/NGF1 for three cycles. As shown in Fig. S6b, the ZIS/NGF1 sample exhibits no apparent deactivation after three cycles, demonstrating the high stability of the composite. Further, no structural difference between the fresh and used catalyst can be seen based on the XRD patterns (Fig. S7).

To clarify the process of photocatalytic CO_2 reduction on ZIS/NGF1, *in-situ* DRIFTS was performed either in dark or under light illumination. Prior to the DRIFTS measurements, the ZIS/NGF1 photocatalyst was degassed at 150°C for 6 h to remove the adsorbed contaminants.
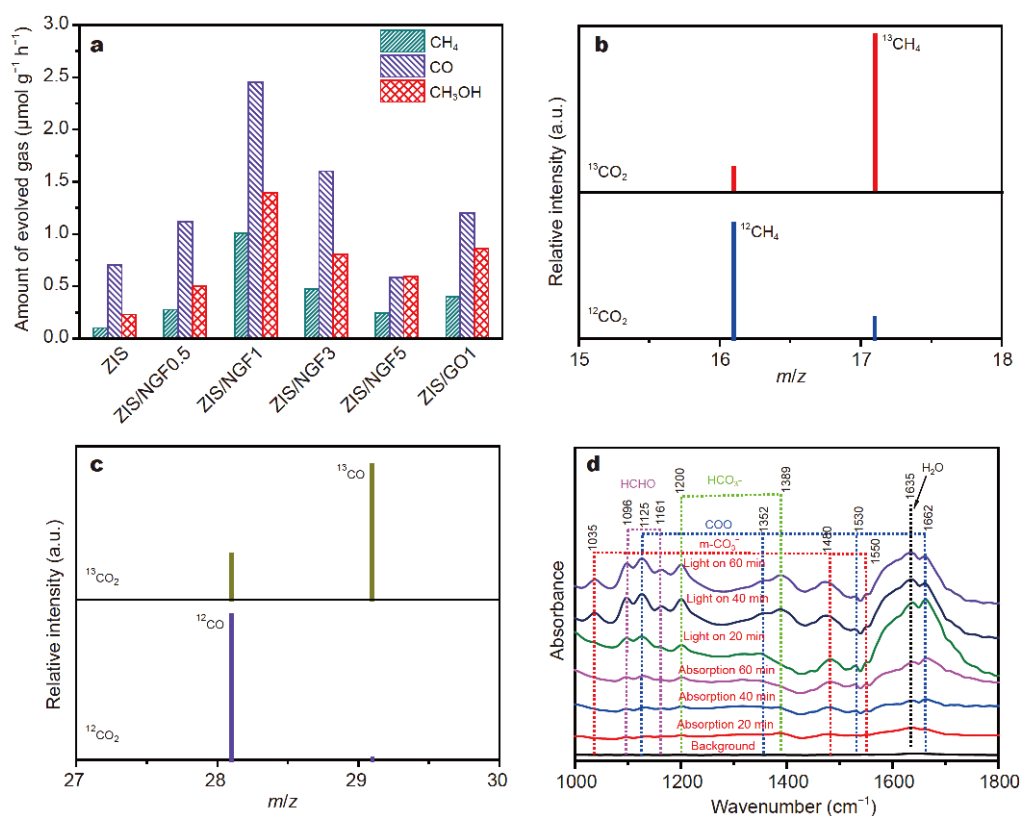
Figure 5 (a) Comparison of different samples in CO_2 photoreduction into CH_4, CO and CH_3OH under simulated sunlight irradiation. (b, c) Reaction products on ZIS/NGF1 analyzed by GC-MS under 300 W Xe lamp irradiation for 1 h with $^{12}CO_2$ and $^{13}CO_2$ as a respective carbon source. (d) *In-situ* DRIFTS spectra of photocatalytic CO_2 reduction by ZIS/NGF1 in dark and under LED light irradiation, respectively.

The IR background spectrum (Fig. 5d) of the photocatalyst was first collected without CO_2 adsorption. When introducing CO_2 onto the photocatalyst, the IR spectra of the adsorbed species were obtained by subtracting the background. Upon exposing CO_2 and H_2O vapor without light illumination, three absorption peaks at 1035, 1480, and 1550 cm^{-1} are ascribed to monodentate carbonate (m-CO_3^{2-}) [24]. The peaks at 1200 and 1389 cm^{-1} result from bicarbonate (HCO_3^{-}) [73]. And the peaks at 1530, 1635 and 1662 cm^{-1} are attributed to bidentate carbonate (b-CO_3^{2-}) and H_2O vapor, respectively [74]. Upon light irradiation, the peaks of m-CO_3^{2-}, b-CO_3^{2-}, HCO_3^{-} become intensive. It is notable that three new peaks at 1125, 1161, and 1352 cm^{-1} for HCHO and HCOO^{-} appear under light irradiation [75]. As a result, the photocatalytic CO_2 reduction on ZIS/NGF1 is shown to be a multi-electron reduction process, involving reaction intermediates such as formic acid and formaldehyde. In addition, CO_2 photoreduction with lower concentration CO_2 and higher concentration N_2 (i.e., 90 vol% of CO_2 replaced by N_2) was carried out. Fig. S8 shows that the

ZIS/NGF1 composite still exhibits good activity, and the respective CH_4, CO and CH_3OH rate is as high as 0.40, 1.15 and 0.52 µmol g^{-1} h^{-1}. Therefore, the unique CO_2 adsorption behavior with high selectivity and strong binding affinity over ZIS/NGF is illustrated, which is a prerequisite for efficient CO_2 photoreduction.

To gain insights into the charge-transfer-capacity capability and dynamics, a series of photo-electro-chemistry measurements were carried out and the results are shown in Fig. 6. The EIS were utilized to probe the interfacial electron-transfer resistance (Fig. 6a). Obviously, the semicircular diameter of Nyquist plot for the ZIS/NGF1 composite is significantly reduced in comparison with ZIS and ZIS/GO1 composite, indicating that the electron-transfer efficiency of the ZIS/NGF1 composite is greater than those of ZIS and ZIS/GO1 composite. The accelerated electron-transfer kinetics in ZIS/NGF1 was also verified by the increased current response in photocurrent measurements (Fig. 6b). Overall, the photocurrent density of ZIS/NGF1 is approximately 1-fold larger than those of ZIS and ZIS/GO1, respectively. To
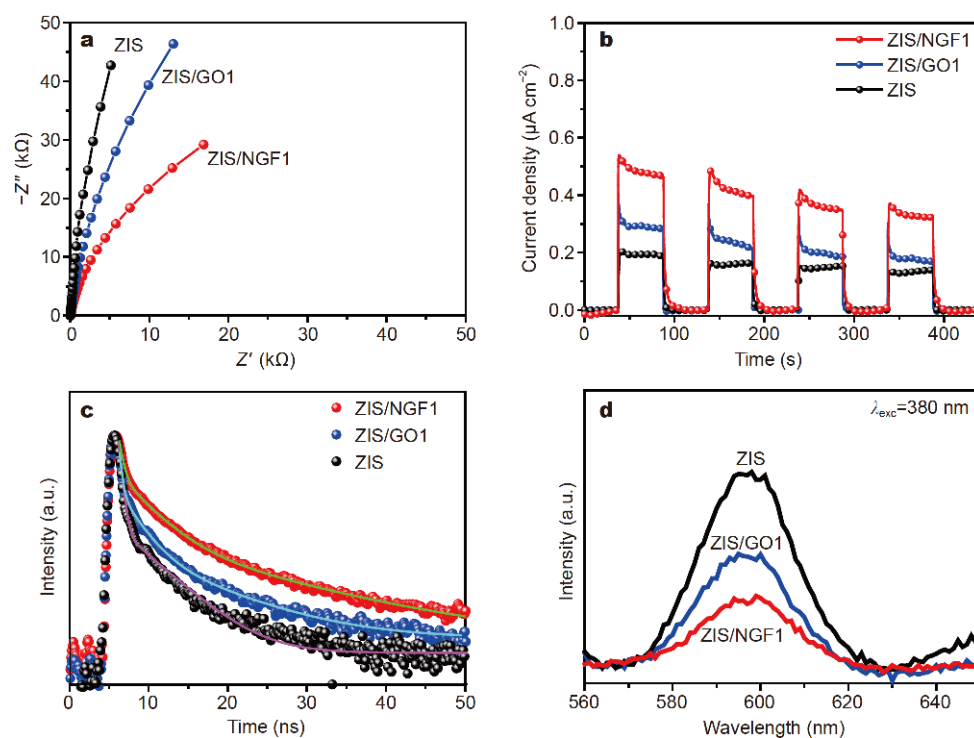
Figure 6 (a) Nyquist plots of EIS. (b) Photoelectrode transient photocurrent response. (c) Time-resolved transient PL decay spectra. (d) Steady-state PL spectra of the ZIS, ZIS/GO1 and ZIS/NGF1 photocatalysts.

analyze the separation and transfer dynamics of the photoexcited charge carriers, TRPL and steady-state PL were employed. TRPL spectra in Fig. 6c show that the decay kinetics of the ZIS/NGF1 composite displays a longer average lifetime (3.13 ns) than those of ZIS (1.64 ns) and ZIS/GO1 (2.84 ns) (Table S4), further suggesting the more efficient charge separation of ZIS/NGF1 composite. The efficient separation of photogenerated carries in ZIS/NGF was further unveiled by PL spectra under 380 nm light excitation. Fig. 6d illustrates that the emission peak at ~ 595 nm of the ZIS/NGF1 composite is suppressed in comparison with ZIS and ZIS/GO1, further proving the effective interfacial charge transfer between ZIS and NGF. The current results based on photo-electro-chemical measurements confirm the superior separation and transfer of photogenerated carries on ZIS/NGF composite, thereby resulting in the excellent performance of photocatalytic CO_2 reduction. In order to explore the pathway of charge transfer across the interface between ZIS and NGF, ISI-XPS measurements were performed under light illumination. As shown in the aforementioned Fig. 3, the binding energies of Zn 2p, In 3d and S 2p core-levels for ZIS/NGF1 show a positive shift of ca. 0.1 eV in comparison with those in dark, suggesting a decrease in electron density on ZIS. On the other hand, the binding

energies of C 1s for ZIS/NGF1 present a negative shift by ca. 0.1 eV as compared with those without light irradiation, implying an increase in electron density on NGF. Therefore, light irradiation is proven to induce the photogenerated electron transfer from ZIS to NGF. Furthermore, the work function measurements were conducted to further investigate the pathway of interfacial charge transfer. Fig. S9 displays the CPDs of NGF, ZIS, and ZIS/NGF1 samples under 461 nm light illumination. The work function (W) of NGF, ZIS, and ZIS/NGF1 is thus determined to be 4.96, 4.57 and 4.62 eV, respectively (inset of Fig. S9). And the Fermi levels (E_f) of the samples are estimated as follows:

$$E_f = E_{vac} - W, \qquad (2)$$

where E_{vac} is the energy of a stationary electron at the vacuum level (assumed as 0 eV), and W is the work function. Accordingly, the E_f of NGF, ZIS and ZIS/NGF1 are calculated to -4.96, -4.57, and -4.62 eV, respectively. Apparently, the E_f of NGF is more nagetive than that of ZIS. When 2D ZIS nanowalls are vertically aligned on the surface of NGF to form hierarchical 2D/3D architecture, the electrons may migrate from ZIS to NGF to achieve Fermi level equilibrium between them. Accordingly, the photoexcited charge carrier migration pathway across the

ZIS/NGF interface is evidenced from ZIS to NGF.

In light of the above results, the photocatalytic process over ZIS/NGF composite is uncovered, aiming to shed light on the enhanced photocatalytic CO_2 reduction over the hierarchical 2D/3D ZIS/NGF composite. The positions of band edges for ZIS and ZIS/NGF were ascertained by XPS valence band (VB) spectra and Mott-Schottky (M-S) plots. As seen in Fig. 7a, the respective VB position of the ZIS and ZIS/NGF1 is 1.84 and 2.17 eV, which can be estimated to be 1.40 and 1.73 V (vs. normal hydrogen electrode, NHE, pH 7.0) using the formula $E_{NHE}/V = V + \Phi - 4.44$ eV (E_{NHE} is the normal hydrogen electrode, Φ is the electron work function (4.00 eV) of the analyzer, V is the valence band maximum) [76]. Furthermore, Fig. 7b displays that the derived flat-band potentials of ZIS and ZIS/NGF1 are −1.08 and −0.75 V (vs. NHE, pH 7.0), respectively. Since the bottom of conduction band (CB) in n-type semiconductors is often more negative by ca. 0.1 V than the flat band potential, the CBs of ZIS and ZIS/NGF1 are determined to be −1.18 and −0.85 V (vs. NHE), respectively. These band energy values are almost in accordance with the ultraviolet photoelectron spectroscopy (UPS) results in Fig. S10. Therefore, the energy band structure and underlying photocatalytic mechanism diagram are illustrated in Fig. 7c. The initial W of NGF is larger than that of ZIS. When ZIS and NGF are coupled with each other, the electron transfer occurs from ZIS to NGF until the Fermi levels are aligned. Thus, a space charge region is formed on the side of ZIS, leading to an upward bending of the energy band. Under simulated sunlight irradiation, electrons are excited from ZIS VB to CB and then transferred to NGF, enabling a further upward bending of the energy band over ZIS. As a result, the photogenerated electrons can barely backflow due to the Schottky barrier. In NGF, the N dopants hold a relatively strong electron affinity to act as polar sites and electron collectors [77], which can attract CO_2 molecules and enable CO_2 to react with photogenerated electrons on the surface of NGF. On the other hand, the holes staying in the VB of ZIS can trigger the oxidation reaction to produce oxygen. To summarize, the hierarchical 2D/3D ZIS/NGF composite is able to facilitate CO_2 uptake as well as the efficient separation of photogenerated charge carriers, and thus boost photocatalytic CO_2 reduction.

CONCLUSIONS
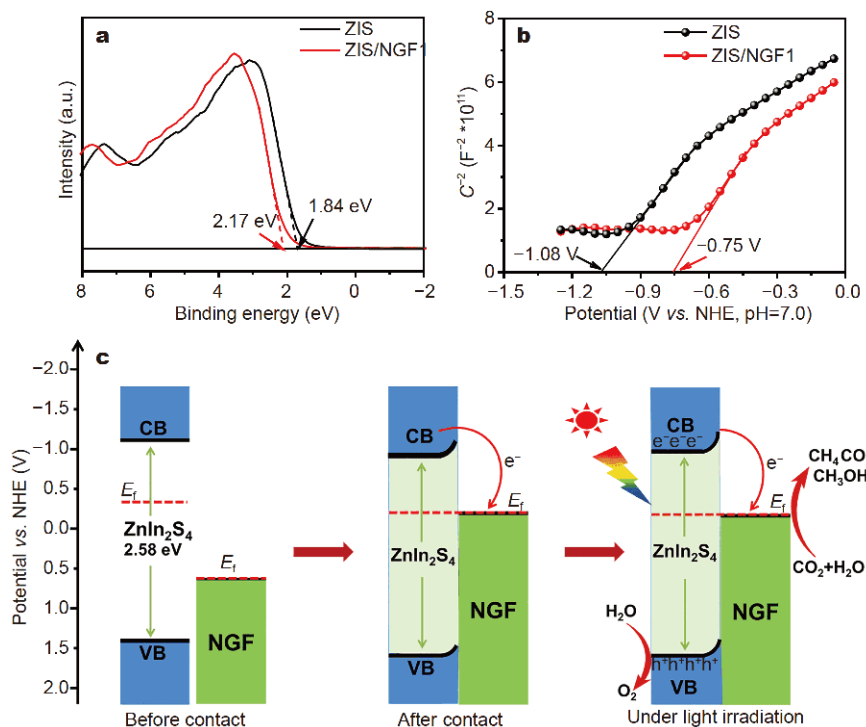
In summary, a near-infrared absorbing 2D/3D ZIS/NGF

Figure 7 (a) The XPS VB spectra of ZIS and ZIS/NGF1. (b) Mott-Schottky plots of ZIS and ZIS/NGF1 at a frequency of 1000 Hz in 0.5 mol L^{-1} Na_2SO_4. (c) Energy level diagram and the photogenerated charge carrier transfer process of NGF and ZIS before and after coupling under simulated sunlight irradiation.

mixed-dimensional composite was hydrothermally prepared by anchoring ZIS nanowalls on the surface of NGF. The ZIS/NGF composite exhibits dramatically enhanced photothermal conversion ability, selective CO_2 capture as well as solar-driven CO_2 photoreduction. In particular, the ZIS/NGF1 composite with 1.0 wt% NGF achieved a comparably high CO_2-to-N_2 selectivity of 30.1 at 273 K and 1 atm, with an isosteric heat of CO_2 adsorption about 48.2 kJ mol^{-1}. Without any cocatalyst and sacrificial agent, under simulated solar light illumination, the ZIS/NGF composite with cyclability converted gas-phase CO_2 into CH_4, CO and CH_3OH, with the respective production rate about 9.1, 3.5, and 5.9 times higher than that of ZIS, which also outperformed typical graphene-based photocatalysts. Nitrogen dopants into the 3D structure of NGF are shown to enlarge the specific surface area and enhance light harvesting, thereby boosting the CO_2 uptake and photothermal conversion efficiency as well as the photogenerated electron-hole pair mobility. In addition, the ZIS/NGF composite-specific architecture presents a highly open conductive network, enhanced CO_2 chemisorption, and strong interfacial coupling, which further facilitates the light absorption, CO_2 uptake, and photoexcited charge transfer across the interface, thereby enhancing the CO_2 reduction under simulated solar light illumination. Furthermore, ISI-XPS combined with work function measurements demonstrated the electron transfer across the heterojunction interface from ZIS to NGF. This work may guide the rational design of hierarchical heterostructures for efficient CO_2 capture and CO_2 photocatalytic conversion.

1 Li X, Yu J, Jaroniec M, et al. Cocatalysts for selective photoreduction of CO_2 into solar fuels. Chem Rev, 2019, 119: 3962–4179

2 Ran J, Jaroniec M, Qiao SZ. Cocatalysts in semiconductor-based photocatalytic CO_2 reduction: achievements, challenges, and opportunities. Adv Mater, 2018, 30: 1704649

3 Han C, Li J, Ma Z, et al. Black phosphorus quantum dot/g-C_3N_4 composites for enhanced CO_2 photoreduction to CO. Sci China Mater, 2018, 61: 1159–1166

4 Low J, Dai B, Tong T, et al. In situ irradiated X-ray photoelectron spectroscopy investigation on a direct Z-scheme TiO_2/CdS composite film photocatalyst. Adv Mater, 2019, 31: 1802981

5 Cao S, Shen B, Tong T, et al. 2D/2D heterojunction of ultrathin MXene/Bi_2WO_6 nanosheets for improved photocatalytic CO_2 reduction. Adv Funct Mater, 2018, 28: 1800136

6 Di T, Xu Q, Ho WK, et al. Review on metal sulphide-based Z-scheme photocatalysts. ChemCatChem, 2019, 11: 1394–1411

7 Zhang N, Long R, Gao C, et al. Recent progress on advanced design for photoelectrochemical reduction of CO_2 to fuels. Sci China Mater, 2018, 61: 771–805

8 Li P, Hou C, Zhang X, et al. Ethylenediamine-functionalized CdS/tetra(4-carboxyphenyl)porphyrin iron(III) chloride hybrid system for enhanced CO_2 photoreduction. Appl Surf Sci, 2018, 459: 292–299

9 Zhou M, Wang S, Yang P, et al. Layered heterostructures of ultrathin polymeric carbon nitride and $ZnIn_2S_4$ nanosheets for photocatalytic CO_2 reduction. Chem Eur J, 2018, 24: 18529–18534

10 Meng A, Zhang L, Cheng B, et al. TiO_2–MnO_x–Pt hybrid multi-heterojunction film photocatalyst with enhanced photocatalytic CO_2-reduction activity. ACS Appl Mater Interfaces, 2019, 11: 5581–5589

11 Crake A, Christoforidis KC, Gregg A, et al. The effect of materials architecture in TiO_2/MOF composites on CO_2 photoreduction and charge transfer. Small, 2019, 15: 1805473

12 Yu S, Wilson AJ, Heo J, et al. Plasmonic control of multi-electron transfer and C–C coupling in visible-light-driven CO_2 reduction on Au nanoparticles. Nano Lett, 2018, 18: 2189–2194

13 Zhou L, Xu YF, Chen BX, et al. Synthesis and photocatalytic application of stable lead-free $Cs_2AgBiBr_6$ perovskite nanocrystals. Small, 2018, 14: 1703762

14 Low J, Zhang L, Zhu B, et al. TiO_2 photonic crystals with localized surface photothermal effect and enhanced photocatalytic CO_2 reduction activity. ACS Sustain Chem Eng, 2018, 6: 15653–15661

15 Li X, Wen J, Low J, et al. Design and fabrication of semiconductor photocatalyst for photocatalytic reduction of CO_2 to solar fuel. Sci China Mater, 2014, 57: 70–100

16 Fu J, Zhu B, Jiang C, et al. Hierarchical porous O-doped g-C_3N_4 with enhanced photocatalytic CO_2 reduction activity. Small, 2017, 13: 1603938

17 Low J, Zhang L, Tong T, et al. TiO_2/MXene Ti_3C_2 composite with excellent photocatalytic CO_2 reduction activity. J Catal, 2018, 361: 255–266

18 Di T, Zhang J, Cheng B, et al. Hierarchically nanostructured porous TiO_2(B) with superior photocatalytic CO_2 reduction activity. Sci China Chem, 2018, 61: 344–350

19 Wang S, Xu M, Peng T, et al. Porous hypercrosslinked polymer-TiO_2-graphene composite photocatalysts for visible-light-driven CO_2 conversion. Nat Commun, 2019, 10: 676

20 Pang R, Teramura K, Asakura H, et al. Highly selective photocatalytic conversion of CO_2 by water over Ag-loaded $SrNb_2O_6$ nanorods. Appl Catal B-Environ, 2017, 218: 770–778

21 Raziq F, Sun L, Wang Y, et al. Synthesis of large surface-area g-C_3N_4 comodified with MnO_x and Au-TiO_2 as efficient visible-light photocatalysts for fuel production. Adv Energy Mater, 2018, 8: 1701580

22 Thanh Truc NT, Hanh NT, Nguyen MV, et al. Novel direct Z-scheme $Cu_2V_2O_7$/g-C_3N_4 for visible light photocatalytic conversion of CO_2 into valuable fuels. Appl Surf Sci, 2018, 457: 968–974

23 Wang S, Guan BY, Lou XWD. Construction of $ZnIn_2S_4$–In_2O_3 hierarchical tubular heterostructures for efficient CO_2 photoreduction. J Am Chem Soc, 2018, 140: 5037–5040

24 Xu F, Zhu B, Cheng B, et al. 1D/2D TiO_2/MoS_2 hybrid nanostructures for enhanced photocatalytic CO_2 reduction. Adv Opt Mater, 2018, 6: 1800911

25 Li H, Gao Y, Zhou Y, et al. Construction and nanoscale detection of interfacial charge transfer of elegant Z-scheme WO_3/Au/In_2S_3 nanowire arrays. Nano Lett, 2016, 16: 5547–5552

26 She H, Zhou H, Li L, et al. Construction of a two-dimensional composite derived from TiO_2 and SnS_2 for enhanced photocatalytic reduction of CO_2 into CH_4. ACS Sustain Chem Eng, 2018, 7: 650–659

27 Cho KM, Kim KH, Park K, et al. Amine-functionalized graphene/

CdS composite for photocatalytic reduction of CO_2. ACS Catal, 2017, 7: 7064–7069

28 Zhu Z, Han Y, Chen C, *et al.* Reduced graphene oxide-cadmium sulfide nanorods decorated with silver nanoparticles for efficient photocatalytic reduction carbon dioxide under visible light. ChemCatChem, 2018, 10: 1627–1634

29 Fu ZC, Xu RC, Moore JT, *et al.* Highly efficient photocatalytic system constructed from CoP/carbon nanotubes or graphene for visible-light-driven CO_2 reduction. Chem Eur J, 2018, 24: 4273–4278

30 Wang Y, Cai Q, Yao M, *et al.* Easy synthesis of ordered mesoporous carbon–carbon nanotube nanocomposite as a promising support for CO_2 photoreduction. ACS Sustain Chem Eng, 2018, 6: 2529–2534

31 Li M, Wang M, Zhu L, *et al.* Facile microwave assisted synthesis of N-rich carbon quantum dots/dual-phase TiO_2 heterostructured nanocomposites with high activity in CO_2 photoreduction. Appl Catal B-Environ, 2018, 231: 269–276

32 Kulandaivalu T, Abdul Rashid S, Sabli N, *et al.* Visible light assisted photocatalytic reduction of CO_2 to ethane using CQDs/Cu_2O nanocomposite photocatalyst. Diamond Related Mater, 2019, 91: 64–73

33 Ye S, Feng J, Wu P. Deposition of three-dimensional graphene aerogel on nickel foam as a binder-free supercapacitor electrode. ACS Appl Mater Interfaces, 2013, 5: 7122–7129

34 Ren L, Hui KS, Hui KN. Self-assembled free-standing three-dimensional nickel nanoparticle/graphene aerogel for direct ethanol fuel cells. J Mater Chem A, 2013, 1: 5689

35 Chen Z, Li H, Tian R, *et al.* Three dimensional graphene aerogels as binder-less, freestanding, elastic and high-performance electrodes for lithium-ion batteries. Sci Rep, 2016, 6: 27365

36 He K, Chen G, Zeng G, *et al.* Three-dimensional graphene supported catalysts for organic dyes degradation. Appl Catal B-Environ, 2018, 228: 19–28

37 Fan Y, Ma W, Han D, *et al.* Convenient recycling of 3D AgX/graphene aerogels (X = Br, Cl) for efficient photocatalytic degradation of water pollutants. Adv Mater, 2015, 27: 3767–3773

38 Wan W, Lin Y, Prakash A, *et al.* Three-dimensional carbon-based architectures for oil remediation: from synthesis and modification to functionalization. J Mater Chem A, 2016, 4: 18687–18705

39 Hasani A, Sharifi Dehsari H, Amiri Zarandi A, *et al.* Visible light-assisted photoreduction of graphene oxide using CdS nanoparticles and gas sensing properties. J Nanomaterials, 2015, 2015: 1–11

40 Li L, He S, Liu M, *et al.* Three-dimensional mesoporous graphene aerogel-supported SnO_2 nanocrystals for high-performance NO_2 gas sensing at low temperature. Anal Chem, 2015, 87: 1638–1645

41 Song Z, Wei Z, Wang B, *et al.* Sensitive room-temperature H_2S gas sensors employing SnO_2 quantum wire/reduced graphene oxide nanocomposites. Chem Mater, 2016, 28: 1205–1212

42 Xia Y, Cui W, Zhang H, *et al.* Synthesis of three-dimensional graphene aerogel encapsulated *n*-octadecane for enhancing phase-change behavior and thermal conductivity. J Mater Chem A, 2017, 5: 15191–15199

43 Han W, Zang C, Huang Z, *et al.* Enhanced photocatalytic activities of three-dimensional graphene-based aerogel embedding TiO_2 nanoparticles and loading MoS_2 nanosheets as co-catalyst. Int J Hydrogen Energy, 2014, 39: 19502–19512

44 Tong Z, Yang D, Shi J, *et al.* Three-dimensional porous aerogel constructed by g-C_3N_4 and graphene oxide nanosheets with excellent visible-light photocatalytic performance. ACS Appl Mater Interfaces, 2015, 7: 25693–25701

45 Song X, Lin L, Rong M, *et al.* Mussel-inspired, ultralight, multi-functional 3D nitrogen-doped graphene aerogel. Carbon, 2014, 80: 174–182

46 Zhao Y, Xie X, Zhang J, *et al.* MoS_2 nanosheets supported on 3D graphene aerogel as a highly efficient catalyst for hydrogen evolution. Chem Eur J, 2015, 21: 15908–15913

47 Ding Y, Gao Y, Li Z. Carbon quantum dots (CQDs) and Co(dmgH)$_2$PyCl synergistically promote photocatalytic hydrogen evolution over hexagonal $ZnIn_2S_4$. Appl Surf Sci, 2018, 462: 255–262

48 Ma J, Wang M, Lei G, *et al.* Polyaniline derived N-doped carbon-coated cobalt phosphide nanoparticles deposited on N-doped graphene as an efficient electrocatalyst for hydrogen evolution reaction. Small, 2018, 14: 1702895

49 Liu B, Ren X, Chen L, *et al.* High efficient adsorption and storage of iodine on S, N co-doped graphene aerogel. J Hazard Mater, 2019, 373: 705–715

50 Duan J, Chen S, Dai S, *et al.* Shape control of Mn_3O_4 nanoparticles on nitrogen-doped graphene for enhanced oxygen reduction activity. Adv Funct Mater, 2014, 24: 2072–2078

51 Zhao X, Wang Z, Xie Y, *et al.* Photocatalytic reduction of graphene oxide-TiO_2 nanocomposites for improving resistive-switching memory behaviors. Small, 2018, 14: 1801325

52 Xia Y, Li Q, Lv K, *et al.* Heterojunction construction between TiO_2 hollowsphere and $ZnIn_2S_4$ flower for photocatalysis application. Appl Surf Sci, 2017, 398: 81–88

53 Ye H, Wang H, Zhang B, *et al.* Tremella-like $ZnIn_2S_4$/graphene composite based photoelectrochemical sensor for sensitive detection of dopamine. Talanta, 2018, 186: 459–466

54 Kale SB, Kalubarme RS, Mahadadalkar MA, *et al.* Hierarchical 3D $ZnIn_2S_4$/graphene nano-heterostructures: their *in situ* fabrication with dual functionality in solar hydrogen production and as anodes for lithium ion batteries. Phys Chem Chem Phys, 2015, 17: 31850–31861

55 Zou H, He B, Kuang P, *et al.* Ni$_x$S$_y$ nanowalls/nitrogen-doped graphene foam is an efficient trifunctional catalyst for unassisted artificial photosynthesis. Adv Funct Mater, 2018, 28: 1706917

56 Xu D, Cheng B, Wang W, *et al.* Ag_2CrO_4/g-C_3N_4/graphene oxide ternary nanocomposite Z-scheme photocatalyst with enhanced CO_2 reduction activity. Appl Catal B-Environ, 2018, 231: 368–380

57 Bin Z, Hui L. Three-dimensional porous graphene-Co_3O_4 nanocomposites for high performance photocatalysts. Appl Surf Sci, 2015, 357: 439–444

58 Jia L, Wang DH, Huang YX, *et al.* Highly durable N-doped graphene/CdS nanocomposites with enhanced photocatalytic hydrogen evolution from water under visible light irradiation. J Phys Chem C, 2011, 115: 11466–11473

59 Chen D, Huang S, Huang R, *et al.* Electron beam-induced microstructural evolution of SnS_2 quantum dots assembled on N-doped graphene nanosheets with enhanced photocatalytic activity. Adv Mater Interfaces, 2019, 6: 1801759

60 Qin W, Han L, Bi H, *et al.* Hydrogen storage in a chemical bond stabilized Co_9S_8–graphene layered structure. Nanoscale, 2015, 7: 20180–20187

61 Song Y, Bai S, Zhu L, *et al.* Tuning pseudocapacitance *via* C–S bonding in WS_2 nanorods anchored on N,S codoped graphene for high-power lithium batteries. ACS Appl Mater Interfaces, 2018, 10: 13606–13613

62 Wei D, Liu Y, Wang Y, *et al.* Synthesis of N-doped graphene by chemical vapor deposition and its electrical properties. Nano Lett, 2009, 9: 1752–1758

63 Liu X, Dong G, Li S, *et al.* Direct observation of charge separation on anatase TiO_2 crystals with selectively etched {001} facets. J Am

Chem Soc, 2016, 138: 2917–2920

64 Xu F, Meng K, Cheng B, et al. Enhanced photocatalytic activity and selectivity for CO_2 reduction over a TiO_2 nanofibre mat using Ag and MgO as Bi-cocatalyst. ChemCatChem, 2019, 11: 465–472

65 Luo C, Zhao J, Li Y, et al. Photocatalytic CO_2 reduction over $SrTiO_3$: Correlation between surface structure and activity. Appl Surf Sci, 2018, 447: 627–635

66 Zhou S, Shang L, Zhao Y, et al. Pd single-atom catalysts on nitrogen-doped graphene for the highly selective photothermal hydrogenation of acetylene to ethylene. Adv Mater, 2019, 31: 1900509

67 Choi HS, Jeon HJ, Choi JH, et al. Tailoring open metal sites for selective capture of CO_2 in isostructural metalloporphyrin porous organic networks. Nanoscale, 2015, 7: 18923–18927

68 Zhao Z, Li Z, Lin YS. Adsorption and diffusion of carbon dioxide on metal−organic framework (MOF-5). Ind Eng Chem Res, 2009, 48: 10015–10020

69 Wang J, Senkovska I, Oschatz M, et al. Imine-linked polymer-derived nitrogen-doped microporous carbons with excellent CO_2 capture properties. ACS Appl Mater Interfaces, 2013, 5: 3160–3167

70 An L, Liu S, Wang L, et al. Novel nitrogen-doped porous carbons derived from graphene for effective CO_2 capture. Ind Eng Chem Res, 2019, 58: 3349–3358

71 Chen J, Yang J, Hu G, et al. Enhanced CO_2 capture capacity of nitrogen-doped biomass-derived porous carbons. ACS Sustain Chem Eng, 2016, 4: 1439–1445

72 Chandra V, Yu SU, Kim SH, et al. Highly selective CO_2 capture on N-doped carbon produced by chemical activation of polypyrrole functionalized graphene sheets. Chem Commun, 2012, 48: 735–737

73 Di T, Zhu B, Cheng B, et al. A direct Z-scheme g-C_3N_4/SnS_2 photocatalyst with superior visible-light CO_2 reduction performance. J Catal, 2017, 352: 532–541

74 Meng A, Wu S, Cheng B, et al. Hierarchical TiO_2/$Ni(OH)_2$ composite fibers with enhanced photocatalytic CO_2 reduction performance. J Mater Chem A, 2018, 6: 4729–4736

75 Xu F, Zhang J, Zhu B, et al. $CuInS_2$ sensitized TiO_2 hybrid nanofibers for improved photocatalytic CO_2 reduction. Appl Catal B-Environ, 2018, 230: 194–202

76 Liu J, Fang W, Wei Z, et al. Efficient photocatalytic hydrogen evolution on N-deficient g-C_3N_4 achieved by a molten salt post-treatment approach. Appl Catal B-Environ, 2018, 238: 465–470

77 Jurca B, Bucur C, Primo A, et al. N-doped defective graphene from biomass as catalyst for CO_2 hydrogenation to methane. ChemCatChem, 2018, 3: cctc.201801984

Author contributions   Yu J, Liu G and Xia Y conceived and designed the experiments. Xia Y carried out the synthesis of the materials and photocatalytic test. Xia Y, Fan J and Cheng B performed the material characterizations. Xia Y, Yu J and Liu G contributed to data analysis. Yu J, Liu G and Cheng B supervised the project. Yu J, Liu G and Xia Y wrote the paper. All authors discussed the results and commented on the manuscript.

Conflict of interest   The authors declare that they have no conflict of interest.

Yang Xia received his MS degree from South Central University for Nationalities in 2017. He is now a PhD candidate under the supervision of Prof. Jiaguo Yu at the State Key Laboratory of Advanced Technology for Materials Synthesis and Processing, Wuhan University of Technology. His current research includes semiconductor photocatalysis, photocatalytic H_2 production, and CO_2 reduction.

Jiaguo Yu received his BS and MS degrees in chemistry from Central China Normal University and Xi'an Jiaotong University, respectively, and his PhD degree in materials science in 2000 from Wuhan University of Technology. In 2000, he became a Professor at Wuhan University of Technology. His current research interests include semiconductor photocatalysis, photocatalytic hydrogen production, CO_2 reduction to hydrocarbon fuels, and so on.

Gang Liu received his PhD degree in 2000 from Texas A&M University, USA. Then he did his postdoctoral work at Brookhaven National Laboratory, University of Pennsylvania and Temple University. He joined the National Center for Nanoscience and Technology, China, in 2007 as an associate professor. His research interests lie in the characterization and properties of a variety of nanoscale materials important in environmental control and clean energy production.

具有近红外吸收的二维/三维$ZnIn_2S_4$/氮掺杂石墨烯光催化剂的制备及其高效CO_2捕获和光催化还原性能

夏阳[1]，程蓓[1]，范佳杰[2]，余家国[1,2*]，刘刚[3*]

摘要   具有宽光谱太阳能利用的分等级异质结光催化剂，正成为一种新兴的先进光催化材料，被应用于太阳能驱动二氧化碳转化为高附加值的化学原料. 本工作通过水热法使二维硫化铟锌纳米墙垂直生长于三维氮掺杂石墨烯泡沫上，形成分等级异质结光催化剂. 该催化剂展现出优异的光热转换效率、选择性捕获CO_2和光催化还原CO_2的能力. 在273 K和1个大气压条件下，负载1 wt% 氮掺杂石墨烯泡沫的复合催化剂表现出最优异的性能，其中对CO_2和N_2的吸附选择性为30.1，并且对CO_2的等量吸附热为48.2 kJ mol^{-1}. 在无助催化剂和牺牲剂的条件下，负载1 wt% 氮掺杂石墨烯泡沫的复合催化剂，其光催化转化CO_2为CH_4、CO和CH_3OH的效率分别是纯的硫化铟锌的9.1、3.5和5.9倍. 该增强效应得益于三维石墨烯泡沫高度开放的网状结构，良好的CO_2吸附能力和两种组份之间的强相互作用. 此外，利用原位照射X射线光电子能谱仪和开尔文探针技术分析了电荷转移的方向，本工作为设计高效太阳能转化分等级异质结光催化剂开辟了新的思路.